

Sustainable oxygen evolution electrocatalysis in aqueous 1 M H₂SO₄ with earth abundant, nanostructured Co₃O₄

Jiahao Yu

Institut Català d'Investigació Química (ICIQ)

Felipe Andrés Garcés

Institute of Chemical Research of Catalonia (ICIQ)

Jesús González-Cobos

Institut Català d'Investigació Química <https://orcid.org/0000-0003-0885-5815>

Maria Peña-Díaz

3Centro de Física de Materiales, CFM/MPC

Celia Rogero

Centro de Física de Materiales (CFM-MPC) Centro Mixto CSIC-UPV/EHU

Sixto Giménez

Jaume I University

Maria Chiara Spadaro

Institut Català de Nanociència i Nanotecnologia <https://orcid.org/0000-0002-6540-0377>

Jordi Arbiol

Catalan Institute of Nanoscience and Nanotechnology (ICN2), CSIC and BIST <https://orcid.org/0000-0002-0695-1726>

Sara Barja

Centro de Física de Materiales (UPV/EHU-CSIC) <https://orcid.org/0000-0002-4257-2651>

Jose Ramon Galan-Mascaros (✉ jrgalan@iciq.es)

Institució Catalana de Recerca i Estudis Avançats <https://orcid.org/0000-0001-7983-9762>

Article

Keywords:

Posted Date: February 8th, 2022

DOI: <https://doi.org/10.21203/rs.3.rs-1317555/v1>

License: © ⓘ This work is licensed under a Creative Commons Attribution 4.0 International License.

[Read Full License](#)

Version of Record: A version of this preprint was published at Nature Communications on July 27th, 2022. See the published version at <https://doi.org/10.1038/s41467-022-32024-6>.

Abstract

Earth-abundant electrocatalysts for the oxygen evolution reaction (OER) able to work in acidic working conditions are elusive. While many first-row transition metal oxides are competitive in alkaline media, most of them just dissolve or become inactive at high proton concentrations where hydrogen evolution is preferred. Only noble metal catalysts, such as IrO₂, are fast and stable enough in acidic media. Herein, we report the excellent activity and long-term stability of Co₃O₄-based anodes in 1 M H₂SO₄ (pH 0.3) when processed in a partially hydrophobic carbon-based protecting matrix. These Co₃O₄@C composites reliably drive O₂ evolution a 10 mA cm⁻² current density for > 40 hours without appearance of performance fatigue, and are the first of their kind to pass benchmarking protocols without incorporating noble metals. Our strategy opens a new venue towards fast, energy efficient acid-media water oxidation electrodes.

Introduction

Hydrogen is considered the most environmentally friendly alternative fuel to replace traditional fossil energy^{1,2}. However, hydrogen production is still dominated worldwide by natural gas steam reforming, a mature technology fixing a very low competitive price in the market. Electrochemical water splitting powered by renewable sources is regarded as the ideal future technology to produce hydrogen, but costs must be lowered to improve its market penetration^{3,4}. The catalysts responsible to improve the efficiency of the process, mainly relying on noble metals, are part of the high cost of the technology, and because of this, many laboratories in the world are working to find viable solutions to develop effective, earth-abundant, robust and scalable catalyst⁵⁻⁸.

Acidic electrolytes offer many advantages for hydrogen production, given that high H⁺ concentration improves the hydrogen evolution reaction (HER), and also facilitates fast/low resistance ionic transport⁹⁻¹⁰. Several electrocatalysts based on low-cost raw materials have shown great promise to substitute the state-of-the-art platinum electrodes responsible for HER^{6,7,11-14}. On the contrary, no viable candidates are known to substitute noble-metal oxides such as IrO₂ at the anode where the oxygen evolution reaction (OER) takes place^{1,6,9,15-21}. So far, no stable and inexpensive OER catalysts can work under high potential and/or current densities in acidic media, where even the highly active RuO₂ presents serious deactivation problems²²⁻²³.

Several strategies have been proposed to promote OER at high proton concentration²⁴⁻²⁸. One strategy deals with the investigation of ternary/complex oxide structures such as nickel-manganese antimonate. This rutile-type oxide was stable for 168 h at 10 mA cm⁻² operating in 1 M sulfuric acid, although with the penalty of requiring a large overpotential ($\eta \geq 700$ mV)²⁶. Cobalt-doped hematite thin-film electrocatalysts were also able to sustain a geometric current density of 10 mA cm⁻² for up to 50 hours at pH 0.3, but again at large overpotentials ($\eta \geq 650$ mV)²⁷. Indeed, cobalt oxides have shown promising OER

electrocatalysis in acidic media, although highly limited by its redox potential-dependent instability, since CoO_x may rapidly dissolve either at open circuit conditions or under high applied potentials^{29–32}. Some interesting advances in long term stability were achieved by doping or processing techniques^{33–35}.

In our previous work with polyoxometalate (POM)-supported catalysts, we disclosed how these molecular catalysts showed remarkable OER catalytic performance in acidic conditions when incorporating active Co centers³⁶. The high activity of these catalysts, even in heterogeneous conditions, was achieved thanks to the synergic stability offered by a partially hydrophobic carbon-based support. However, this strategy was not successful to achieve long-term stability, since these POM-based electrodes could only survive at low current densities and for a very limited time, given their intrinsic instability to the mechanical stress provoked by gas bubbling.

In this work, we present a novel processing protocol which combines in one single anode two powerful strategies: i) the incorporation of a nanostructured OER catalyst from earth abundant metals to maximize active surface area, ii) supported by a conducting, partially hydrophobic binder made from paraffin oil and graphite powder. Our processing protocol with nitrogen-doped carbon-coated Co_3O_4 nanoparticles ($\text{Co}_3\text{O}_4@\text{C}$) delivers robust and scalable anodes that exhibit excellent acidic OER performances, needing a minimum overpotential ($\eta \leq 398$ mV) to maintain a 10 mA cm^{-2} current density for > 40 hours when working in 1 M sulfuric acid solution, without any sign of fatigue or deactivation. The high activity and also great stability demonstrate a performance superior to any other non-noble catalysts reported. Oxygen evolution quantification confirms the Faradaic efficiency (> 96%) of these electrodes towards OER, with negligible participation of other oxidation processes. These results open new opportunities for stable OER electrocatalysis with earth abundant raw materials.

Results

Catalyst and electrode preparation

The overall synthetic and processing protocol is summarized in Figure 1. We synthesized carbon-coated Co ($\text{Co}@\text{C}$) nanoparticles, starting from the thermal treatment of $\text{Co}(\text{blm})_2$ ($\text{blm} = 2\text{-benzimidazolate}$), a metal-organic framework (MOF) precursor (ZIF-9)³⁷. Then $\text{Co}@\text{C}$ was oxidized at low-temperature to achieve its full transformation into cobalt oxide nanoparticles, covered by an amorphous, nitrogen doped-carbon coating derived from the organic skeleton ($\text{Co}_3\text{O}_4@\text{C}$, Figure 1). Powder X-ray diffraction (PXRD) patterns and Raman spectra confirmed the presence of a Co_3O_4 phase and the carbon support (Figures S1–S4). High-resolution transmission electron microscopy (HRTEM) the presence of graphitic-like nanostructures all around the sample, embedding the Co_3O_4 nanoparticles. Some of these C-nanostructures had a nanosheet-like morphology (Figure 2), while some others were folded forming onion-like rings around the Co_3O_4 nanoparticles (Figure S5). Electron energy loss spectroscopy in scanning TEM mode (EELS-STEM) confirmed the chemical composition of the nanoparticles and

surrounding nanostructures (Figure S6). The $\text{Co}_3\text{O}_4@\text{C}$ composition was determined as $(\text{Co}_3\text{O}_4)(\text{H}_2\text{O})_{0.30}(\text{OH})_{0.85}\text{C}_{2.00}\text{N}_{0.05}$ by thermogravimetry elemental analysis (Figure S7 and Table S1).

For the preparation of the electrode composites, $\text{Co}_3\text{O}_4@\text{C}$ was mixed with graphite (G) and paraffin oil (PO) in the desired ratio (see Methods section) to prepare a homogeneous composite ($\text{Co}_3\text{O}_4@\text{C}/\text{GPO}$) with the desired $\text{Co}_3\text{O}_4@\text{C}$ content up to 40% (40- $\text{Co}_3\text{O}_4@\text{C}$). Composites above 40% were mechanically too fragile for further processing into the working electrode pocket. HRTEM images and EELS-STEM maps showed the similar nanostructures within $\text{Co}_3\text{O}_4@\text{C}/\text{GPO}$ and close contact between $\text{Co}_3\text{O}_4@\text{C}$ and GPO (Figure 2 and Figure S8). X-ray photoemission spectroscopy (XPS) analysis was employed to further identify the surface chemical composition and the mixed oxidation state $\text{Co}^{2+/3+}$ (Figure S9) consistent with the presence of the Co_3O_4 , as confirmed by PXRD and HRTEM data³⁸. XPS spectra from the $\text{Co}_3\text{O}_4@\text{C}/\text{GPO}$ composite show no differences respect to the $\text{Co}_3\text{O}_4@\text{C}$ precursor, demonstrating the absence of chemical modification during composite preparation.

OER electrocatalytic activity in 1 M H_2SO_4

The $x\text{-Co}_3\text{O}_4@\text{C}/\text{GPO}$ composites (x corresponds to the % in weight for the metal oxide) were inserted into the pocket of a working electrode and used as anode during electrochemical water oxidation in 1 M H_2SO_4 ($\text{pH} \approx 0.3$). The cyclic voltammetry (CV) showed the appearance of a catalytic current density on the $\text{Co}_3\text{O}_4@\text{C}/\text{GPO}$ electrode at relatively low overpotentials, which was sustained after successive cycling curves (Figure S10). Comparative linear sweep voltammetry (LSV) showed an enhanced electrochemical activity upon increasing $\text{Co}_3\text{O}_4@\text{C}$ content, reaching a very low onset overpotential ($\eta_{\text{onset}} = 190$ mV) for the 40- $\text{Co}_3\text{O}_4@\text{C}/\text{GPO}$ electrode (Figure 3). These electrodes reach 10 mA cm^{-2} currents at just ≥ 356 mV overpotential. Interestingly, no sign of a transport-limited regime appeared in the studied potential range, reaching over 20 mA cm^{-2} at $\eta \geq 393$ mV.

We prepared analogous IrO_2/GPO working electrodes to benchmark our results in the same conditions with the state-of-the-art IrO_2 . The IrO_2/GPO anodes delivered higher overpotentials, $\eta_{j=10\text{mAcm}^{-2}} = 368$ mV at 10 mA cm^{-2} and $\eta_{j=20\text{mAcm}^{-2}} = 396$ mV at 20 mA cm^{-2} , slightly above those obtained for the $\text{Co}_3\text{O}_4@\text{C}$ -based electrode (Table S2). This competitive activity becomes even more significant if we normalize current density per gram of catalyst (Figure 3c).

Tafel analyses of the LSV data yielded slopes of 139 mV dec^{-1} for $\text{Co}_3\text{O}_4@\text{C}$ and 83 mV dec^{-1} for IrO_2 (Figure 3d), suggesting a different reaction mechanism (rate-limiting step) for these two catalysts, and indicating a faster increment of current density with the applied potential for IrO_2 ^{39,40}. Interestingly, this is compensated by the lower onset potential of $\text{Co}_3\text{O}_4@\text{C}/\text{GPO}$. The electrochemical double-layer capacitance (EDLC) of $\text{Co}_3\text{O}_4@\text{C}/\text{GPO}$ and IrO_2/GPO were calculated as 25 and 2 mF cm^{-2} , respectively, with 0.03 mF cm^{-2} for the blank GPO (Figure S11), respectively. This indicates a greater electrochemical active surface area for $\text{Co}_3\text{O}_4@\text{C}/\text{GPO}$, due to its higher density of active sites in $\text{Co}_3\text{O}_4@\text{C}/\text{GPO}$, thanks

to is nano-structuration, favouring the higher current densities observed in the potential range studied^{41, 42}.

Finally, we measured anodic oxygen evolution during chronopotentiometry experiments with $\text{Co}_3\text{O}_4@\text{C}/\text{GPO}$ electrodes (Figure S12). We found over >96% Faradaic efficiency, confirming that OER is the dominant process at these electrodes' surface, and confirming no significant oxidation of the carbon-based matrix is taking place in these conditions.

OER electrocatalytic stability in 1 M H_2SO_4

As mentioned before, stability is a critical issue for earth abundant OER catalysts in acidic media⁴³⁻⁴⁷. To determine the stability of our $\text{Co}_3\text{O}_4@\text{C}/\text{GPO}$ electrodes, we take advantage of the benchmarking protocol designed by Jaramillo's group^{6,48} that uses as figure of merit the overpotential required to achieve and maintain a 10 mA cm^{-2} current density per geometric area at ambient temperature after two hours of continuous water electrolysis. The corresponding chronopotentiometry data (Figure 4a-c) show very good stability for all electrodes, independently of their $\text{Co}_3\text{O}_4@\text{C}$ content. In all cases, $\eta_{j=10\text{mAcm}^{-2}}$ after 2 hours shows just a small increment. In the case of our best electrodes, the 40- $\text{Co}_3\text{O}_4@\text{C}/\text{GPO}$, this increment is of just 3 mV, and the stability is maintained for long times. After 43 h of continuous electrolysis, the overpotential is essentially identical to the starting value (Figure 4a).

The benchmarking of these electrodes with previous literature is highlighted in the $\eta_{j=10\text{mAcm}^{-2}, t=2\text{h}}$ vs $\eta_{j=10\text{mAcm}^{-2}, t=0\text{h}}$ plot (Figure 4d). This comparative plot illustrates the high activity and stability of our electrodes. The three of them appear at the diagonal of the graph, as expected for sustainable performance, and very close and competitive to the results obtained with noble metal counterparts. For the first time, earth abundant anodes successfully pass this benchmarking protocol for OER performance in acidic media.

Stability number (S-number) and Activity-Stability Factor (ASF) were also proposed as key metrics for estimating lifetime and long-term stability for electrocatalysts⁴⁹⁻⁵¹. Thus, we analyzed the electrolyte after stability tests to check for Co leaching (Table S3). We found the presence of Co but at the ppb level, corresponding to just $\approx 0.4\%$ of the total. Based on this number, we can estimate a 25 S-number, an ASF of 101 and a lifetime of 462 h. These estimations are comparable even to Ir-based catalysts such as SrIrO_3 in analogous conditions, and confirm the promising performance/stability of these electrodes. It is worthy to mention that this small Co loss does not significantly affect performance. So we assign it essentially to catalytically non-active areas.

Post-electrolysis $\text{Co}_3\text{O}_4@\text{C}/\text{GPO}$ characterization

To further confirm the stability of $\text{Co}_3\text{O}_4@\text{C}$ as a genuine OER catalyst, we characterized the structural and chemical evolution of the electrodes after these 2 h electrolysis at 10 mA cm^{-2} in 1 M H_2SO_4 . The powder XRD patterns did not show any significant change nor shift in the observed peaks, still typical of

Co₃O₄@C and graphite (Figure S13). This suggests no major structural changes are occurring to the bulk of the material Co₃O₄@C.

We explored potential changes on the chemical composition of the catalyst due to OER process by XPS characterization of the fresh electrode and after water electrolysis under different conditions. The Co 2p XPS spectrum of the fresh Co₃O₄@C/GPO electrode (Figure 5a) shows two peaks located at 794.9 eV (Co 2p_{1/2}) and 779.7 eV (Co 2p_{3/2}), corresponding to the spin-orbit splitting of the 2p orbital. Both components contain equivalent chemical information. The deconvoluted analysis of the peaks reveals the presence of two different chemical components, which we attribute to the Co³⁺ (blue) and Co²⁺ (green) states, in agreement with the presence of Co₃O₄³⁸. In addition, we observe two doubled satellite peaks arising from charge transfer and final states effects from Co²⁺ (satellite A, yellow) and Co³⁺ (satellite B, red),⁵² again characteristic of Co₃O₄. We also analyzed the O 1s peak (Figure 5a). In addition to the Co-O component (brown) related to the Co₃O₄, we observe a higher binding energy component attributed to residual OH/H₂O (pink). Quantitative analysis of the Co 2p and O 1s core levels of Co₃O₄@C/GPO after chronopotentiometry at 10 mA cm⁻² for 2 h (Figure 5b) and 5 mA cm⁻² for 24 h (Figure 5c) revealed no shifts in the binding energies of the components respect to the fresh sample. Crucially, the main spectral features attributed to a Co₃O₄@C catalyst remain unaltered after water electrolysis, which demonstrates the preservation of the oxidation state of the catalyst. Changes in the intensity of the OH/H₂O component on the O 1s can be fairly attributed to the different environmental conditions of the emersed electrode (see Experimental section). XPS analysis of the C component does not evidence significant changes in the oxidation state of the C 1s peak, supporting the preservation of the carbon-based matrix (Figure S14) in agreement to the obtained Faradaic efficiencies. Nitrogen detection in the system is below our resolution limit; therefore, no discussion is referred to this element. Based on the current analysis, the most important finding is that the oxide film is stable and no cobalt oxide is lost nor further oxidized during the electrolysis process. In summary, XRD and XPS strongly support the bulk and surface stability of Co₃O₄@C during acidic OER electro catalysis, and its genuine catalytic activity.

We also investigated the Co₃O₄@C/GPO composite after 2 h electrolysis at 10 mA cm⁻² by means of HR-TEM (Figure 6). The images and power spectra (FFT) analyses also confirm a high structural and chemical stability. Neither crystallinity nor particle size are affected by the electrochemical process.

Critical role of GPO

To investigate the actual role of the carbon paste in the stability of the electrodes, we carried out additional alternative experiments. First, we directly deposited Co₃O₄@C on a glassy carbon (GC) electrode. This electrode showed a significantly lower electrocatalytic activity when compared with the Co₃O₄@C/GPO (Figure 3-4 vs Figure S15). More importantly, after 30-min of the benchmarking test in 1 M

H₂SO₄, the Co₃O₄@C/GC electrode is apparently deactivated. This suggests that the GPO binder is fundamental to confer the acidic stability and activity of the Co₃O₄@C component.

This effect of the GPO binder could be due to a modified local pH at the electrode/electrolyte interface⁵³⁻⁵⁵. To check this hypothesis, we decided to investigate the effect of the GPO binder on the local pH through the reversible H⁺/H₂ pair as catalyzed with commercial Pt/C⁵⁶. The reversible potential for this model reaction differs when the Pt/C is directly deposited on a graphite electrode, or when incorporated into a GPO electrode as observed in their CV plots in a hydrogen saturated 1 M H₂SO₄ electrolyte (Figure S16). An average value of + 0.001 V vs E_{RHE} was estimated for the Pt/C catalyst, in good agreement with the theoretical +0.0 V value. A +0.06 V vs E_{RHE} was found for the (Pt/C)/GPO electrode. If we associate this potential difference to the local pH, $\Delta E = 0.059 \Delta \text{pH}$, we can estimate a pH difference of 1 unit between both electrodes, which does not immediately explain the higher stability obtained for the GPO electrodes under acidic water oxidation conditions. Therefore, we associate the protective function essentially to the hydrophobicity environment, which avoids proper solvation of the oxides, precluding its dissolution.

We also compared the activity/stability of Co₃O₄@C vs Co₃O₄ (Figure S15). The corresponding x-Co₃O₄/GPO electrodes showed good stability during preliminary CV cycles and chronopotentiometry measurement, but at higher overpotentials. A 5 mF cm⁻² EDLC was determined, just 1/5 that of Co₃O₄@C/GPO (Figure S11). Specific surface area from N₂ sorption isotherm curves for Co₃O₄@C was also about 5 times greater than that of Co₃O₄ (Figure S17). These results suggest that the role of the carbon coating is to improve the nanostructuring of the active Co₃O₄ material.

In addition, the Co₃O₄@C/GPO, Co₃O₄/GPO and IrO₂/GPO electrodes were studied by Electrochemical Impedance Spectroscopy (EIS) at different applied potentials. Figure S18 shows the obtained Nyquist plots, which systematically feature two arcs (or distorted arc for IrO₂), consistent with two simultaneous/consecutive charge-transfer channels⁵⁷. Fitting the experimental data to a suitable equivalent circuit model (Figure S18) revealed that the best ohmic contact (reflected by the series resistance, R_s) is obtained for the Co₃O₄@C/GPO (Figure S19a). On the other hand, the charge transfer resistance (R_{ct}), scales inversely with the electrocatalytic activity of the different electrodes, being the lowest one for the Co₃O₄@C/GPO electrode (Figure S19b). This is consistent with the estimated surface capacitance, which scales with electrode performance, as a result of higher surface area and hence, higher density of catalytic sites (Figure S19c).

Discussion

The discussion may contain subheadings and can in some cases be combined with the results section. In summary, we are reporting the high activity and promising stability of carbon-decorated Co₃O₄@C nanoparticles (Co₃O₄@C) for electrocatalytic OER under acidic conditions when protected by a hydrophobic binder support. Electrodes built from Co₃O₄@C, graphite and paraffin oil are able to evolve

oxygen from water during the electrolysis of a concentrated (1 M) sulfuric acid solution (pH < 0.3). These anodes are the first ones to successfully pass the benchmarking protocol established in acidic media OER,⁶ without containing noble metals (neither Ir nor Ru).

Although previous reports on acidic water splitting with earth-abundant raw materials had achieved either high activity or high stability, this is the first consistent report of a working anode fulfilling both requirements (Table S4). These electrodes operate during more than 40 h, at a relatively high current density (10 mA cm⁻²) and at a low overpotential of $\eta < 398$ mV, very close to the benchmarking performance of state-of-the-art IrO₂.

The synergy between active catalytic phase, Co₃O₄ nanoparticles, and the carbon support (doped-carbon cover, graphite and paraffin oil) is crucial to reach this robust performance. Despite the promising performance of our electrodes, a few challenges will need to be addressed before their implementation into commercial electrolyzers. To start with, the carbon content may become an issue at high current densities, as those expected from commercial devices (> 500 mA cm⁻²). But our successful corrosion-protection opens an interesting strategy that can be translated into full cell devices, looking for alternative approaches to incorporate hydrophobic species at the electrode surfaces.

In addition, it is worthy to mention that the current densities reached and sustained by the Co₃O₄@C/GPO electrodes are high enough to satisfy the needs of photoelectrochemical (PEC) devices, well in line with the maximum currents provided by photoanodes. Investigations to combine these acid-stable electrodes as co-catalyst for photoactive semi-conductors are under way.

Methods

Materials and chemicals

All the chemical reagents and solvents were of commercial grade and used directly without any further purification Experimental Details.

Synthesis

ZIF-9 was prepared via a solvothermal method according to the previous literature with some modifications^{58, 59}. Co(NO₃)₂·6H₂O (0.175 g) and benzimidazole (0.142 g) were dissolved into 15 mL DMF and then the homogeneous solution was transferred into a Teflon-lined stainless autoclave. The sealed autoclave was put into an oven and kept at 140 °C for 24 h. When it was cooled down to room temperature, the purple product was filtered out and washed with acetone, and then dried at 60 °C.

To obtain the target material, Co@C was firstly synthesized using ZIF-9 as precursor by heating at 500 and then 750 °C for 2 h, respectively, under Ar flow. Afterwards, the pyrolysis product was oxidized in air at 230 °C for 48 h to generate Co₃O₄@C.

The composite electrodes were prepared by 2-hour ball-milling at 20 s^{-1} of a mixture of paraffin oil (20 mg), graphite powder (80 mg) and the desired weight of metal oxide (5, 10, 20, 30 or 40 mg), namely, $x\text{-Co}_3\text{O}_4\text{@C/GPO}$. $x\text{-IrO}_2\text{/GPO}$ and $x\text{-Co}_3\text{O}_4\text{/GPO}$ electrodes were also prepared for comparison purposes.

Structural characterization

Powder X-ray diffraction (PXRD) data were recorded with a Bruker D8 Advance Series equipped with a VANTEC-1 PSD3 detector. Elemental analyses were carried out with an Agilent 725-ES inductively coupled plasma optical emission spectrometer (ICP-OES) at University of Valladolid (Co) and LECO CHNS-932 elementary microanalyzers (C, H, N) at Complutense University of Madrid. Thermogravimetric analysis was conducted with a thermogravimetric balance of Mettler Toledo. Nitrogen adsorption-desorption isotherms at 77 K were measured on a Quantachrome Autosorb iQ gas adsorption analyzer. Prior to analysis, the sample was degassed in vacuum. The BET method was applied to calculate the total surface area.

Electrochemistry

All electrochemical experiments were performed under ambient conditions with a Bio-Logic VMP3 multichannel potentiostat and implemented with a three-electrode configuration using 1 M H_2SO_4 (pH 0.3) as filling solution, Pt mesh as counter electrode, Ag/AgCl (3 M KCl) as reference electrode and a pocket working electrode (0.07 cm^2 surface area and 4 mm depth) filled with the GPO composites. The actual mass amounts of the $x\text{-Co}_3\text{O}_4\text{@C/GPO}$ composites in the electrode pocket were measured with a weight balance and are indicated in Table S5. Although it is difficult to estimate the actual active layer, an estimation is suggested that 1/8 of the total electrode pocket volume is used as the maximum limit in contact with the solution in order to determine the mass loading for comparison³⁶. All potentials were measured versus Ag/AgCl electrode and converted to the RHE reference scale using $E_{\text{RHE}} = E_{\text{Ag/AgCl}} + 0.21 + 0.059 \text{ pH}$ (V) while overpotentials $\eta = E_{\text{RHE}} - 1.229 \text{ V}$. All current densities were calculated based on the geometrical surface area of the electrodes. Ohmic drop was determined for all electrochemical data by using the automatic current interrupt (CI) software, and the corresponding ohmic drops are included in Table S5. All LSV experiments were carried out with a 1 mV s^{-1} scan rate and CV experiments with 10 mV s^{-1} . Tafel slopes were estimated from the LSV curves by plotting overpotential η vs $\log j$ (j = current density). The potential vs RHE to drive 1 mA cm^{-2} was used to define onset potential and corresponding η_{onset} . Chronopotentiometry tests were carried out at fixed current densities of 10 mA cm^{-2} . For the electrochemical double-layer capacitance (EDLC) measurements, open circuit potentials (OCPs) vs. the Ag/AgCl were firstly recorded for 30 mins to reach rather stable values. Combined with above CV measurements, the 100 mV potential windows centered at OCPs could be determined and cyclic voltammeteries were then carried out under scanning rates of 20, 40, 60, 80 and 100 mV s^{-1} . The current density differences between the minimum and maximum values at OCPs vs. the Ag/AgCl and the corresponding scanning rates were plotted to calculate the EDLC value (1/2 of the slope of current

density-scan rate plots)⁶⁰. Co₃O₄@C and commercial Pt/C were also deposited on the glassy carbon (GC, 0.07 cm²) disk electrodes. The inks were prepared by sonicating 10 mg of catalyst, 25 μL Nafion 117 containing solution and 975 μL ethanol aqueous solution (3:1 in volume) for 30 mins.

High Electrochemical impedance spectroscopy (EIS) was performed by means of a typical three-electrode cell in the frequency range from 100 kHz to 0.1 Hz with 8 points per decade. The AC perturbation was 5 mV. Experimental data were fitted to the selected equivalent circuit model using Zview software (Scriber Associates) for extracting both capacitances and resistances.

Faradaic efficiency

In order to evaluate the faradaic efficiency towards oxygen production, the chronopotentiometric experiment was carried out applying a fixed current while oxygen concentration in the headspace was in-situ measured by using an Unisense sensing system equipped with an oxygen microsensor based on voltage polarization. The experiment was performed under continuous flow conditions by bubbling Ar as carrier gas in both anodic and cathodic compartments. For this purpose, an H-type cell was used containing a frit glass separating both compartments, a connection for the sensor to be inserted in the anodic gas headspace, and connections for the inlet and outlet Ar streams in both compartments (Figure S20). The oxygen microsensor was in situ two-point calibrated by feeding to the H-cell with certified standard of Ar (≥ 99.999%) and compressed air, being the gas flow rate controlled by a set of mass flowmeters (Bronkhorst EL-FLOW).

After purging the cell headspace with argon, the chronopotentiometry test was started and the oxygen concentration was monitored until reaching stabilization. The expected faradaic oxygen production rate is calculated with the following equation:

$$F_{O_2, far} = I n_e^{-1} F^{-1} \quad (1)$$

Where I is the applied current (in A), n_e is the number of mols of electrons involved in the water oxidation reaction to generate one mol of oxygen (4) and F is the Faraday constant (96485 C mol⁻¹).

The experimental O₂ flow rate was calculated considering ideal gas behavior with the following equation:

$$F_{O_2, exp} = P C_{O_2} F_{Ar} (100 - C_{O_2})^{-1} R^{-1} T^{-1} \quad (2)$$

Where P is the total gas pressure (1 atm), $C(O_2)$ is the steady-state oxygen concentration provided by the sensor (in %), F_{Ar} is the Ar carrier flow, R is the ideal gas constant (0.082 atm L K⁻¹ mol⁻¹) and T is the cell temperature (293 K).

Then Faradaic efficiency (in %), FE , is calculated as follows:

$$FE = \frac{100 \times F_{O_2,exp}}{F_{O_2,far}} \quad (3)$$

X-ray photoemission spectroscopy

X-Ray photoemission (XPS) experiments were performed inside an ultra-high vacuum chamber (base pressure of 10^{-10} mbar) using a Phoibos 100 photoelectron spectrometer equipped with an Al K α X-ray source (16 mA, 1486.6 V) as the incident photon radiation. XPS spectra of Co 2p, O 1s, N 1s, and C 1s core levels were measured for as received samples deposited on top of indium tape. The spectra are well described by the superposition of several Doniach-Sunjic curve-components. The intensities of the XPS core levels were evaluated by the peak areas, after a standard background subtraction according to Shirley procedure⁶¹. The spin-orbit splitting for every component into the Co-2p core level has been set to $D = 15.2$ eV with a branching ratio of 0.5. The metallic cobalt peak, Co 2p_{3/2}=779.7 eV, was used for a final calibration of the spectra.³⁸ Co₃O₄@C/GPO after OER chronopotentiometry at 10 mA·cm⁻² for 2h at was washed with acetone in order to remove the paraffin oil prior to XPS measurements. As expected, the treatment do not affect the oxidation state of the composite, as evidenced by the measured spectra.

Transmission electron microscopy

High resolution transmission electron microscopy (HRTEM) and scanning transmission electron microscopy (STEM) investigations were performed on a field emission gun FEI Tecnai F20 microscope. High angle annular dark-field (HAADF) STEM was combined with electron energy loss spectroscopy (EELS) in the Tecnai microscopy by using a GATAN QUANTUM energy filter in order to obtain compositional maps. STEM-EELS maps were performed using the O K-edge at 532 eV (green), the Co L-edge at 779 eV (red) and C K-edge at 284 eV (blue).

Declarations

Acknowledgements

The authors thank the support from projects RED2018-102459-T, RTI2018-095618-B-I00 and PID2020-116093RB-C41,C43&C44, funded by MCIN/AEI/10.13039/501100011033/ and by “ERDF A way of making Europe”; the Generalitat de Catalunya (2017-SGR-1406 and 2017-SGR-327), and the IKERTALDE 2019 (consolidated research groups, IT-1255-19). J.Y. thanks the China Scholarship Council (CSC) for predoctoral fellowships (File No. 201806270234). S.B. acknowledges RyC program RYC-2017-21931 and UPV/EHU project EHUroPE19/01 and IKERBASQUE, Basque Foundation for Science. ICIQ and ICN2 are supported by the Ministerio de Ciencia e Innovación through the Severo Ochoa Excellence Accreditations CEX2019-000925-S (MIC/AEI) and SEV-2017-0706; and by the CERCA Programme/Generalitat de Catalunya. M.C.S. has received funding from the European Union’s Horizon 2020 research and innovation programme under Marie Skłodowska-Curie grant 754510 (PROBIST) and the Severo Ochoa program.

Author contributions

J.R.G.M conceived the original concept and with S.B. designed the project and coordinated the efforts of the research team. J.Y. synthesized, processed and structurally characterized the materials and electrodes. J.Y. and F.G.P. characterized the compounds electrochemically and analyzed the data. J.Y. and J.G.C. measured the oxygen evolution. M.P.D., C.R. and S.B. collected and analyzed the XPS data. M.C.S. and J. A. collected and analyzed the TEM data. S. G. collected and analyzed the EIS data. J.Y., S.B. and J.R.G.M. co-wrote the manuscript with contributions from all authors.

Competing interests

The authors declare no competing interests.

Correspondence

Correspondence and requests for materials should be addressed to Sara Barja (sara.barja@ehu.eus) and José Ramón Galán-Mascarós (jrgalan@iciq.es).

References

1. Wei, C. *et al.* Recommended Practices and Benchmark Activity for Hydrogen and Oxygen Electrocatalysis in Water Splitting and Fuel Cells. *Adv. Mater.* **31**, 1–24 (2019).
2. Staffell, I. *et al.* The role of hydrogen and fuel cells in the global energy system. *Energy Environ. Sci.* **12**, 463–491 (2019).
3. Singh, S. *et al.* Hydrogen: A sustainable fuel for future of the transport sector. *Renew. Sustain. Energy Rev.* **51**, 623–633 (2015).
4. Sharma, S. & Ghoshal, S. K. Hydrogen the future transportation fuel: From production to applications. *Renew. Sustain. Energy Rev.* **43**, 1151–1158 (2015).
5. Seh, Z. W. *et al.* Combining theory and experiment in electrocatalysis: Insights into materials design. *Science* **355**, 1–12 (2017).
6. McCrory, C. C. L. *et al.* Benchmarking Hydrogen Evolving Reaction and Oxygen Evolving Reaction Electrocatalysts for Solar Water Splitting Devices. *J. Am. Chem. Soc.* **137**, 4347–4357 (2015).
7. Zhu, J., Hu, L., Zhao, P., Lee, L. Y. S. & Wong, K. Y. Recent Advances in Electrocatalytic Hydrogen Evolution Using Nanoparticles. *Chem. Rev.* **120**, 851–918 (2020).
8. Lyu, F., Wang, Q., Choi, S. M. & Yin, Y. Noble-Metal-Free Electrocatalysts for Oxygen Evolution. *Small* **15**, 1–17 (2019).
9. Spöri, C., Kwan, J. T. H., Bonakdarpour, A., Wilkinson, D. P. & Strasser, P. The Stability Challenges of Oxygen Evolving Catalysts: Towards a Common Fundamental Understanding and Mitigation of Catalyst Degradation. *Angew. Chemie - Int. Ed.* **56**, 5994–6021 (2017).

10. Han, B. *et al.* Screening Oxide Support Materials for OER Catalysts in Acid. *J. Electrochem. Soc.* **165**, 813–820 (2018).
11. Chung, D. Y. *et al.* Large-Scale Synthesis of Carbon-Shell-Coated FeP Nanoparticles for Robust Hydrogen Evolution Reaction Electrocatalyst. *J. Am. Chem. Soc.* **139**, 6669–6674 (2017).
12. Schipper, D. E. *et al.* Effects of Catalyst Phase on the Hydrogen Evolution Reaction of Water Splitting: Preparation of Phase-Pure Films of FeP, Fe₂P, and Fe₃P and Their Relative Catalytic Activities. *Chem. Mater.* **30**, 3588–3598 (2018).
13. Sun, J. *et al.* Robust Hydrogen-Evolving Electrocatalyst from Heterogeneous Molybdenum Disulfide-Based Catalyst. *ACS Catal.* **10**, 1511–1519 (2020).
14. Yu, J., Cheng, G. & Luo, W. Ternary nickel-iron sulfide microflowers as a robust electrocatalyst for bifunctional water splitting. *J. Mater. Chem. A* **5**, 15838–15844 (2017).
15. Kuo, D. Y. *et al.* Influence of Surface Adsorption on the Oxygen Evolution Reaction on IrO₂ (110). *J. Am. Chem. Soc.* **139**, 3473–3479 (2017).
16. Cherevko, S. *et al.* Oxygen and hydrogen evolution reactions on Ru, RuO₂, Ir, and IrO₂ thin film electrodes in acidic and alkaline electrolytes: A comparative study on activity and stability. *Catal. Today* **262**, 170–180 (2016).
17. Chen, S. *et al.* Mn-Doped RuO₂ Nanocrystals as Highly Active Electrocatalysts for Enhanced Oxygen Evolution in Acidic Media. *ACS Catal.* **10**, 1152–1160 (2020).
18. Shan, J., Zheng, Y., Shi, B., Davey, K. & Qiao, S. Z. Regulating electrocatalysts via surface and interface engineering for acidic water electrooxidation. *ACS Energy Lett.* **4**, 2719–2730 (2019).
19. Escudero-Escribano, M. *et al.* Importance of Surface IrO_x in Stabilizing RuO₂ for Oxygen Evolution. *J. Phys. Chem. B* **122**, 947–955 (2018).
20. Seitz, L. C. *et al.* A highly active and stable IrO_x/SrIrO₃ catalyst for the Oxygen evolution reaction. *Science* **353**, 1011–1014 (2016).
21. Ouattara, L., Fierro, S., Frey, O., Koudelka, M. & Comninellis, C. Electrochemical comparison of IrO₂ prepared by anodic oxidation of pure iridium and IrO₂ prepared by thermal decomposition of H₂IrCl₆ precursor solution. *J. Appl. Electrochem.* **39**, 1361–1367 (2009).
22. Lyons, M. E. G. & Floquet, S. Mechanism of oxygen reactions at porous oxide electrodes. Part 2 - Oxygen evolution at RuO₂, IrO₂ and Ir_xRu_{1-x}O₂ electrodes in aqueous acid and alkaline solution. *Phys. Chem. Chem. Phys.* **13**, 5314–5335 (2011).
23. Stoerzinger, K. A. *et al.* Orientation-Dependent Oxygen Evolution on RuO₂ without Lattice Exchange. *ACS Energy Lett.* **2**, 876–881 (2017).
24. Rodríguez-García, B. *et al.* Cobalt hexacyanoferrate supported on Sb-doped SnO₂ as a non-noble catalyst for oxygen evolution in acidic medium. *Sustain. Energy Fuels* **2**, 589–597 (2018).
25. Li, A. *et al.* Stable Potential Windows for Long-Term Electrocatalysis by Manganese Oxides Under Acidic Conditions. *Angew. Chem. Int. Ed.* **58**, 5054–5058 (2019).

26. Moreno-Hernandez, I. A. *et al.* Crystalline nickel manganese antimonate as a stable water-oxidation catalyst in aqueous 1.0 M H₂SO₄. *Energy Environ. Sci.* **10**, 2103–2108 (2017).
27. Kwong, W. L., Lee, C. C., Shchukarev, A. & Messinger, J. Cobalt-doped hematite thin films for electrocatalytic water oxidation in highly acidic media. *Chem. Commun.* **55**, 5017–5020 (2019).
28. Zhou, L. *et al.* Rutile Alloys in the Mn–Sb–O System Stabilize Mn³⁺ to Enable Oxygen Evolution in Strong Acid. *ACS Catal.* **8**, 10938–10948 (2018).
29. Chatti, M. *et al.* Intrinsically stable in situ generated electrocatalyst for long-term oxidation of acidic water at up to 80°C. *Nat. Catal.* **2**, 457–465 (2019).
30. Bloor, L. G., Molina, P. I., Symes, M. D. & Cronin, L. Low pH electrolytic water splitting using earth-abundant metastable catalysts that self-assemble in situ. *J. Am. Chem. Soc.* **136**, 3304–3311 (2014).
31. Mondschein, J. S. *et al.* Crystalline Cobalt Oxide Films for Sustained Electrocatalytic Oxygen Evolution under Strongly Acidic Conditions. *Chem. Mater.* **29**, 950–957 (2017).
32. Etzi Coller Pascuzzi, M., van Velzen, M., Hofmann, J. P. & Hensen, E. J. M. On the Stability of Co₃O₄ Oxygen Evolution Electrocatalysts in Acid. *ChemCatChem* **13**, 459–467 (2021).
33. Yang, X. *et al.* Highly acid-durable carbon coated Co₃O₄ nanoarrays as efficient oxygen evolution electrocatalysts. *Nano Energy* **25**, 42–50 (2016).
34. Yan, K. L. *et al.* Probing the active sites of Co₃O₄ for the acidic oxygen evolution reaction by modulating the Co²⁺/Co³⁺ ratio. *J. Mater. Chem. A* **6**, 5678–5686 (2018).
35. Etzi Coller Pascuzzi, M., van Velzen, M., Hofmann, J. P. & Hensen, E. J. M. On the Stability of Co₃O₄ Oxygen Evolution Electrocatalysts in Acid. *ChemCatChem* **13**, 459–467 (2021).
36. Arens, J. T. *et al.* Water oxidation electrocatalysis in acidic media with Co-containing polyoxometalates. *J. Catal.* **389**, 345–351 (2020).
37. Park, K. S. *et al.* Exceptional chemical and thermal stability of zeolitic imidazolate frameworks. *Proc. Natl. Acad. Sci. U. S. A.* **103**, 10186–10191 (2006).
38. Biesinger, M. C. *et al.* Resolving surface chemical states in XPS analysis of first row transition metals, oxides and hydroxides: Cr, Mn, Fe, Co and Ni. *Appl. Surf. Sci.* **257**, 2717–2730 (2011).
39. Anantharaj, S. *et al.* Recent Trends and Perspectives in Electrochemical Water Splitting with an Emphasis on Sulfide, Selenide, and Phosphide Catalysts of Fe, Co, and Ni: A Review. *ACS Catal.* **6**, 8069–8097 (2016).
40. Reier, T., Oezaslan, M. & Strasser, P. Electrocatalytic oxygen evolution reaction (OER) on Ru, Ir, and Pt catalysts: A comparative study of nanoparticles and bulk materials. *ACS Catal.* **2**, 1765–1772 (2012).
41. Li, D., Shi, J. & Li, C. Transition-Metal-Based Electrocatalysts as Cocatalysts for Photoelectrochemical Water Splitting: A Mini Review. *Small* **14**, 1–22 (2018).
42. Tamirat, A. G., Rick, J., Dubale, A. A., Su, W. N. & Hwang, B. J. Using hematite for photoelectrochemical water splitting: A review of current progress and challenges. *Nanoscale*

- Horizons **1**, 243–267 (2016).
43. Reier, T., Nong, H. N., Teschner, D., Schlögl, R. & Strasser, P. Electrocatalytic Oxygen Evolution Reaction in Acidic Environments – Reaction Mechanisms and Catalysts. *Adv. Energy Mater.* **7**, 1601275 (2017).
 44. Ashton, S. J. & Arenz, M. A DEMS study on the electrochemical oxidation of a high surface area carbon black. *Electrochem. commun.* **13**, 1473–1475 (2011).
 45. Hu, Q. *et al.* Coupling pentlandite nanoparticles and dual-doped carbon networks to yield efficient and stable electrocatalysts for acid water oxidation. *J. Mater. Chem. A* **7**, 461–468 (2019).
 46. Cheng, W. *et al.* A metal-vacancy-solid-solution NiAlP nanowall array bifunctional electrocatalyst for exceptional all-pH overall water splitting. *J. Mater. Chem. A* **6**, 9420–9427 (2018).
 47. Mondschein, J. S. *et al.* Intermetallic Ni₂Ta Electrocatalyst for the Oxygen Evolution Reaction in Highly Acidic Electrolytes. *Inorg. Chem.* **57**, 6010–6015 (2018).
 48. McCrory, C. C. L., Jung, S., Peters, J. C. & Jaramillo, T. F. Benchmarking heterogeneous electrocatalysts for the oxygen evolution reaction. *J. Am. Chem. Soc.* **135**, 16977–16987 (2013).
 49. Geiger, S. *et al.* The stability number as a metric for electrocatalyst stability benchmarking. *Nat. Catal.* **1**, 508–515 (2018).
 50. Kim, Y. T. *et al.* Balancing activity, stability and conductivity of nanoporous core-shell iridium/iridium oxide oxygen evolution catalysts. *Nat. Commun.* **8**, 1–8 (2017).
 51. An, L. *et al.* Recent Development of Oxygen Evolution Electrocatalysts in Acidic Environment. *Adv. Mater.* **33**, 1–31 (2021).
 52. Díaz-Fernández, D. *et al.*, The growth of cobalt oxides on HOPG and SiO₂ surfaces: A comparative study. *Surface Science* **624**, 145–153 (2014).
 53. Wang, J., Musameh, M. & Mo, J. W. Acid stability of carbon paste enzyme electrodes. *Anal. Chem.* **78**, 7044–7047 (2006).
 54. Fang, Z. *et al.* Hybrid Organic-Inorganic Gel Electrocatalyst for Stable Acidic Water Oxidation. *ACS Nano* **13**, 14368–14376 (2019).
 55. Sempionatto, J. R. *et al.* Enzymatic biofuel cells based on protective hydrophobic carbon paste electrodes: Towards epidermal bioenergy harvesting in the acidic sweat environment. *Chem. Commun.* **56**, 2004–2007 (2020).
 56. Liang, Y. *et al.* Co₃O₄ nanocrystals on graphene as a synergistic catalyst for oxygen reduction reaction. *Nat. Mater.* **10**, 780–786 (2011).
 57. Han, L. *et al.* Cobalt Hexacyanoferrate as a Selective and High Current Density Formate Oxidation Electrocatalyst. *ACS Appl. Energy Mater.* **3**, 9198–9207 (2020).
 58. Yang, F., Chen, Y., Cheng, G., Chen, S. & Luo, W. Ultrathin Nitrogen-Doped Carbon Coated with CoP for Efficient Hydrogen Evolution. *ACS Catal.* **7**, 3824–3831 (2017).
 59. Yang, F. *et al.* Design of active and stable oxygen reduction reaction catalysts by embedding Co_xO_y nanoparticles into nitrogen-doped carbon. *Nano Res.* **10**, 97–107 (2017).

60. Morales, D. M. & Risch, M. Seven steps to reliable cyclic voltammetry measurements for the determination of double layer capacitance. *J. Phys. Energy* **3**, 34013 (2021).
61. Shirley, D. A. High-resolution X-ray photoemission spectrum of the valence bands of gold. *Phys. Rev. B* **5**, 4709–4714 (1972).

Figures

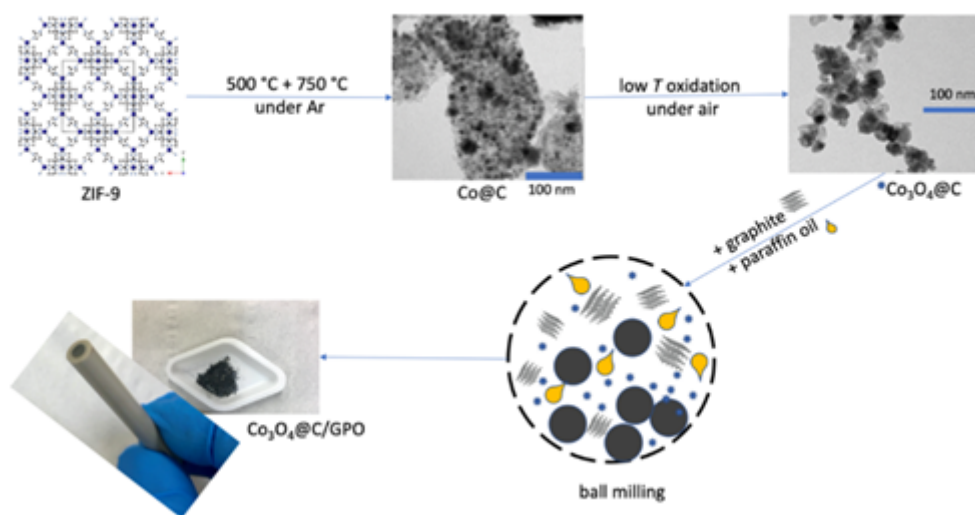


Figure 1

Scheme of the synthesis and processing of a $\text{Co}_3\text{O}_4@\text{C}/\text{GPO}$ electrode.

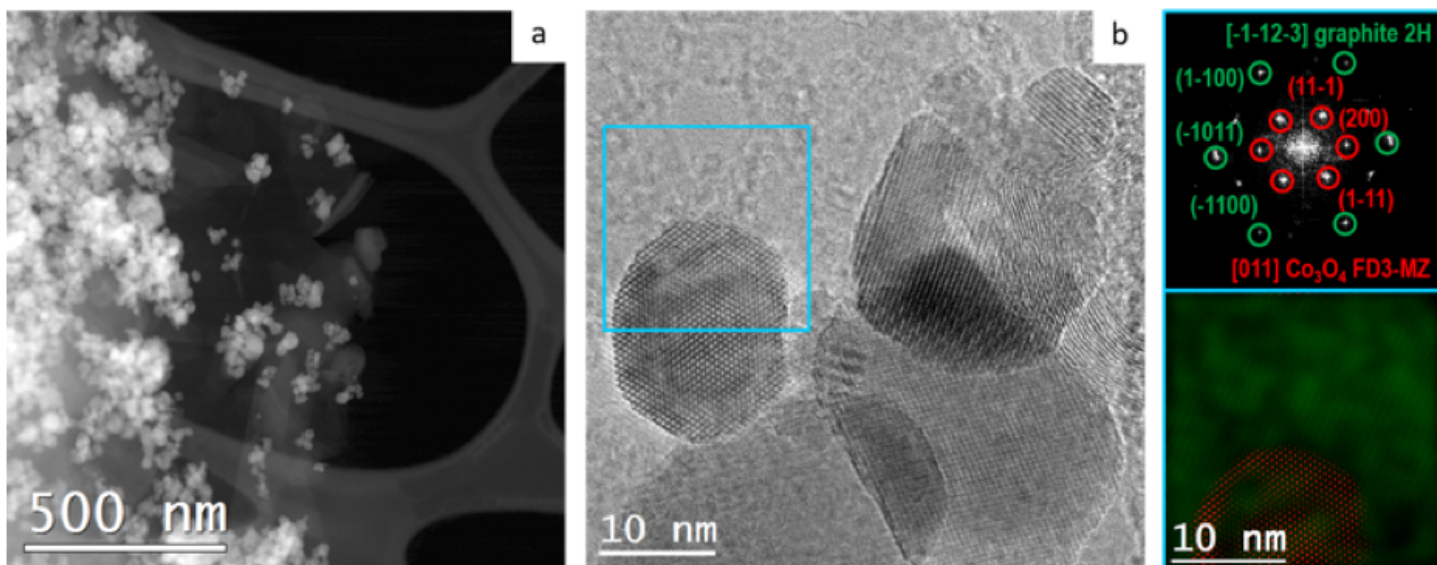


Figure 2

HAADF STEM (a) and HRTEM (b) micrographs from a fresh $\text{Co}_3\text{O}_4@\text{C}/\text{GPO}$ composite. The power spectrum analysis confirms the presence of Co_3O_4 nanoparticles with a cubic FD3-MZ (s.g. 227) spinel structure, oriented along its [011] axis, superimposed to the reflections corresponding to graphite layers with a ≈ 0.34 nm spacing and here oriented along the $[-1-12-3]$. To highlight the different systems, we show a frequency filtered map (on the bottom right) where the Co_3O_4 corresponding lattice fringes are in red and the graphite layer ones in green.

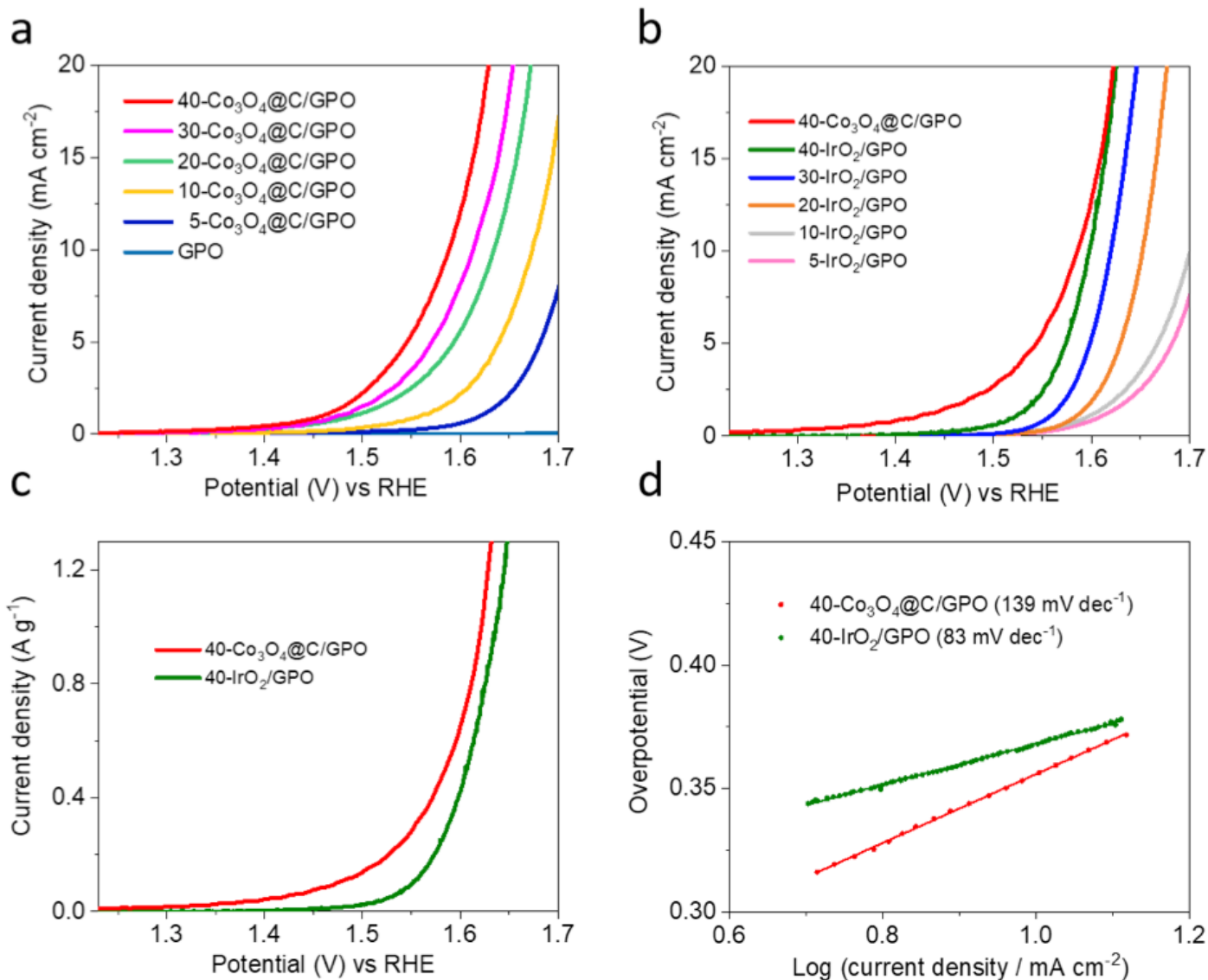


Figure 3

Electrolysis electrocatalytic activity of the $\text{Co}_3\text{O}_4@\text{C}/\text{GPO}$ in 1 M H_2SO_4 electrolyte. (a) LSV curves for $x\text{-Co}_3\text{O}_4@\text{C}/\text{GPO}$ ($x = 5, 10, 20, 30, 40$) electrodes in 1 M H_2SO_4 (pH 0.3) with 1 mV s^{-1} scan rate; (b) LSV curves of $x\text{-IrO}_2/\text{GPO}$ ($x = 5, 10, 20, 30, 40$) with contrast to $40\text{-Co}_3\text{O}_4@\text{C}/\text{GPO}$; (c) comparative overpotential dependence of the mass-normalized current density of IrO_2/GPO and $\text{Co}_3\text{O}_4@\text{C}/\text{GPO}$; (d) Tafel plots of IrO_2/GPO and $\text{Co}_3\text{O}_4@\text{C}/\text{GPO}$ extracted from LSV data.

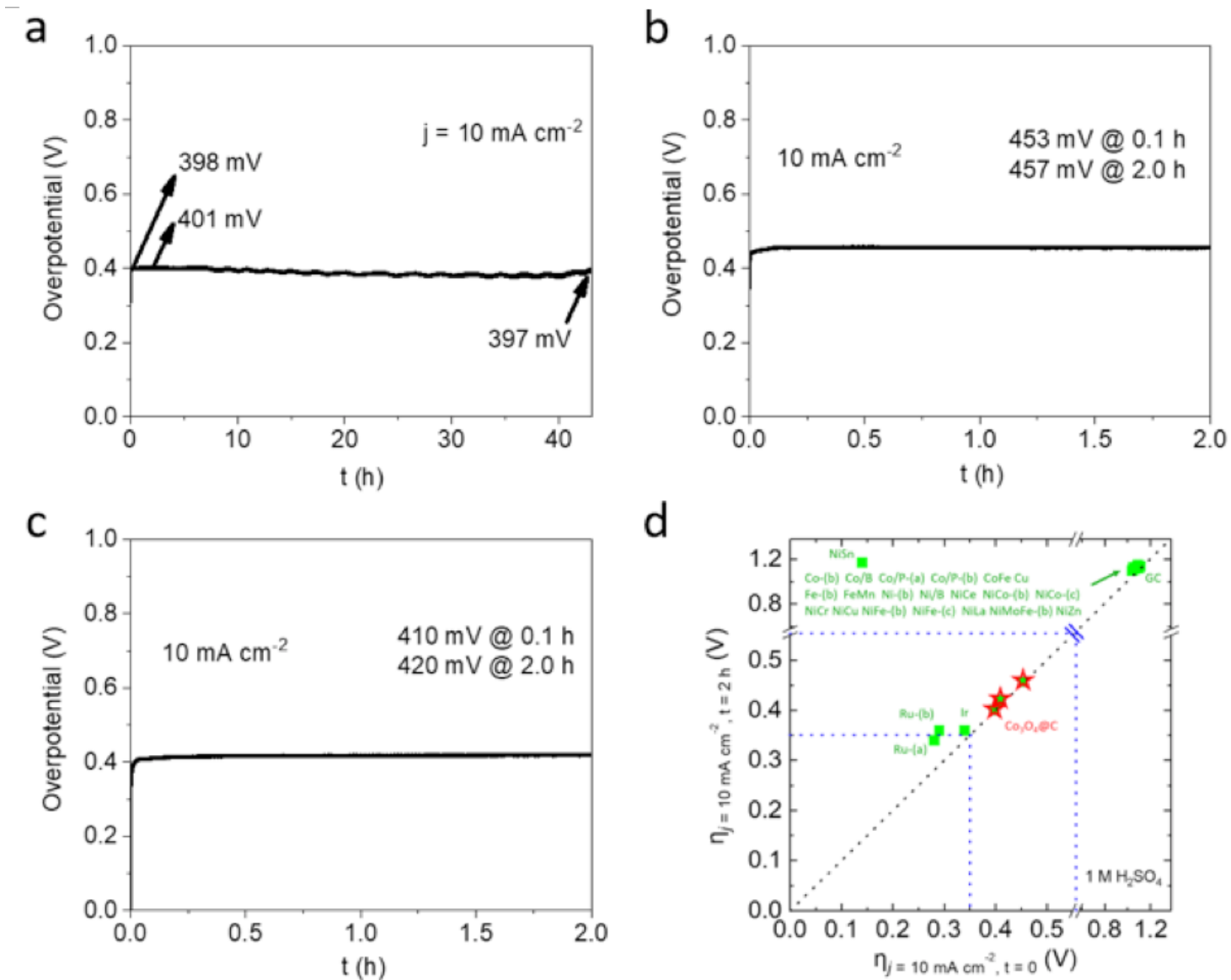


Figure 4

Stability of the $\text{Co}_3\text{O}_4@\text{C}/\text{GPO}$ electrodes in chronopotentiometry measurements at 10 mA cm^{-2} in $1 \text{ M H}_2\text{SO}_4$ electrolyte. (a) $40\text{-Co}_3\text{O}_4@\text{C}/\text{GPO}$ (> 40 hours). (b) $20\text{-Co}_3\text{O}_4@\text{C}/\text{GPO}$ (2 hours). (c) $30\text{-Co}_3\text{O}_4@\text{C}/\text{GPO}$ (2 hours). (d) benchmarking of their activity/stability features (red stars) in comparison with other OER electrocatalysts (green squares) in the same electrolysis conditions according to the data from a previous benchmarking study⁶.

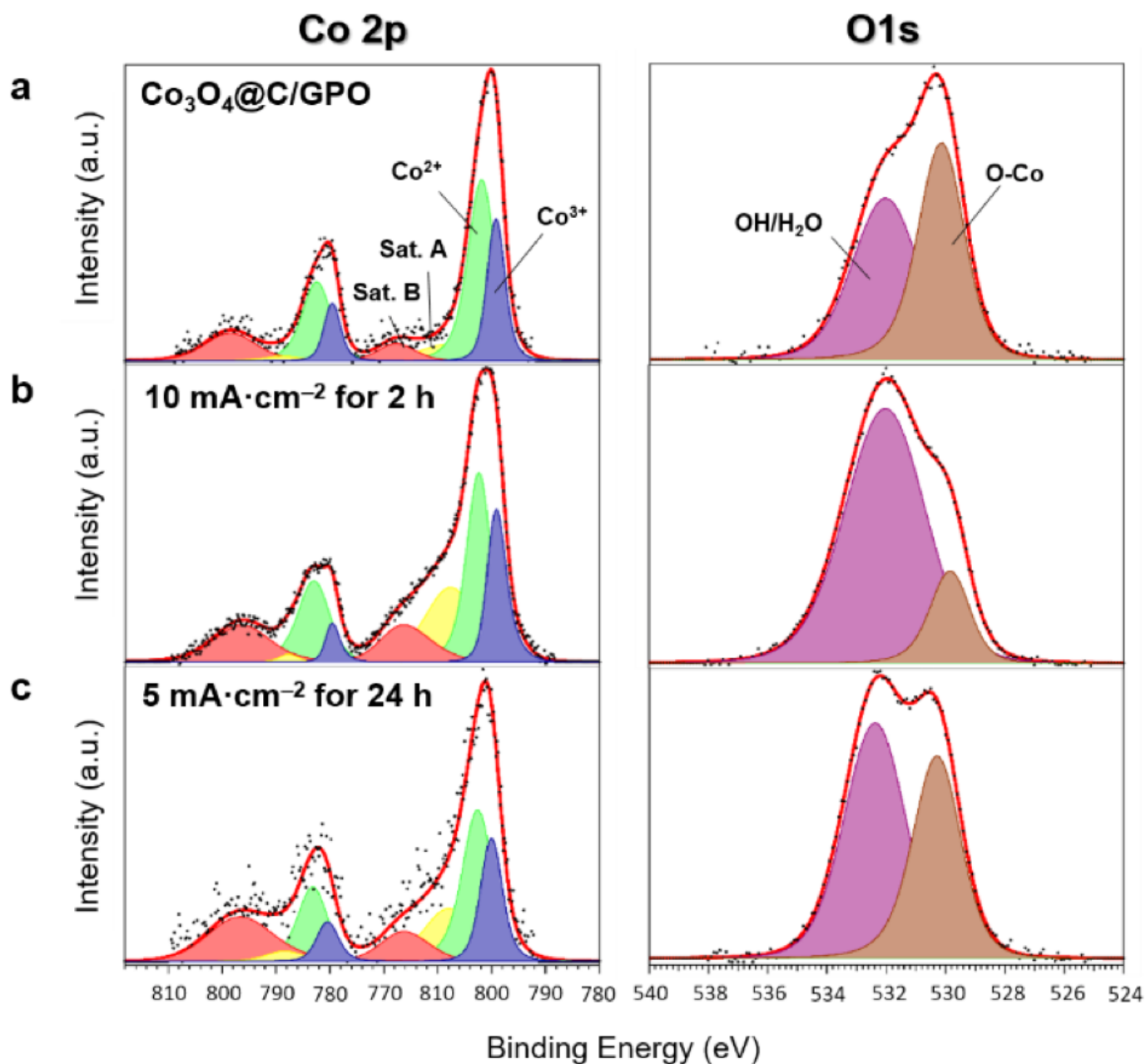


Figure 5

Chemical analysis of the $\text{Co}_3\text{O}_4@\text{C}/\text{GPO}$ catalyst after water electrolysis. (a) X-ray photoelectron spectra of the Co 2p (left) and O 1s (right) core levels for a 20- $\text{Co}_3\text{O}_4@\text{C}/\text{GPO}$ electrode. (b) same spectra for a 20- $\text{Co}_3\text{O}_4@\text{C}/\text{GPO}$ electrode after OER chronopotentiometry at 10 mA cm^{-2} for 2 h. (c) same spectra for a 20- $\text{Co}_3\text{O}_4@\text{C}/\text{GPO}$ electrode after OER chronopotentiometry at 5 mA cm^{-2} for 24 h.

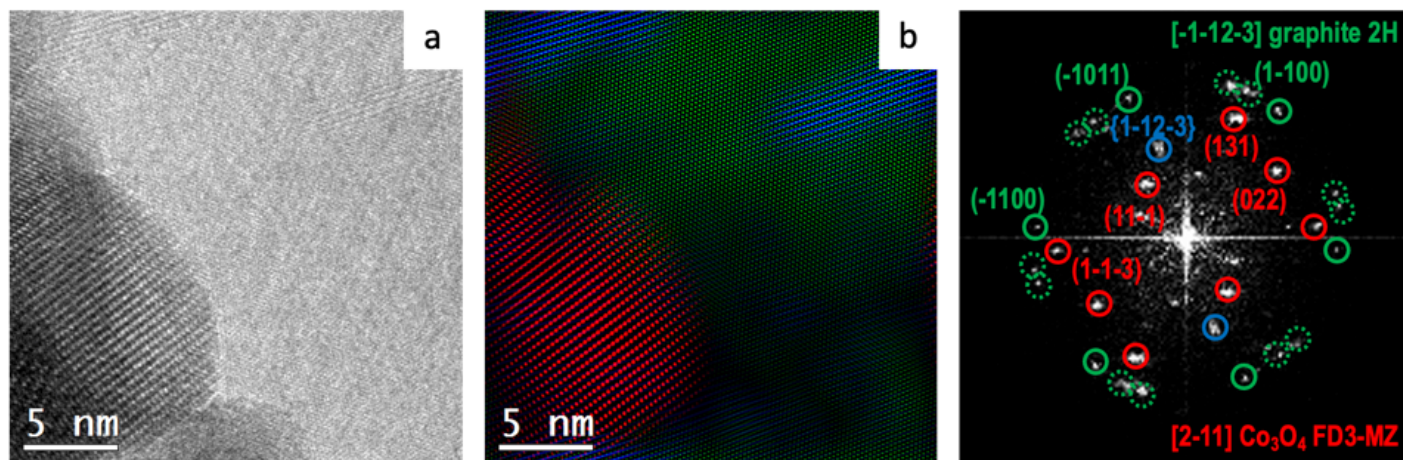


Figure 6

HRTEM micrograph (a) from a $\text{Co}_3\text{O}_4@\text{C}/\text{GPO}$ composite, recovered after 2 h water electrolysis at 10 mA cm^{-2} . To highlight the different systems, we show a frequency filtered map (b) where the Co_3O_4 nanoparticle lattice fringes are in red and the ones corresponding to the surrounding graphitic layers in green and blue. The power spectra (FFT) confirm the high stability of these electrodes, showing again Co_3O_4 nanoparticles with a cubic FD3-MZ (s.g. 227) spinel structure here oriented along the $[2-11]$ zone axis. No changes in crystallinity or particle size are observed for the $\text{Co}_3\text{O}_4@\text{C}$ composite when compared to the fresh samples (Figure 2). Notice that the graphitic layers may show multiple rotated domains as shown by the highlighted dotted green circles in the power spectrum, but this effect also happened in the as-prepared sample.

Supplementary Files

This is a list of supplementary files associated with this preprint. Click to download.

- [Nat.comunsi.docx](#)